

Atomic-resolution studies of epitaxial strain release mechanisms in $\text{La}_{1.85}\text{Sr}_{0.15}\text{CuO}_4/\text{La}_{0.67}\text{Ca}_{0.33}\text{MnO}_3$ superlattices

N. Biškup,^{1,2} S. Das,³ J. M. Gonzalez-Calbet,^{4,2} C. Bernhard,³ and M. Varela¹

¹*Departamento de Física Aplicada III, Instituto Pluridisciplinar, Universidad Complutense de Madrid, Spain*

²*Centro Nacional de Microscopía Electrónica, Universidad Complutense de Madrid, Spain*

³*Department of Physics, Fribourg Center for Nanomaterials, University of Fribourg, Chemin du Musée 3, CH-1700 Fribourg, Switzerland*

⁴*Departamento de Química Inorgánica, Universidad Complutense de Madrid, Spain*

(Received 17 December 2014; revised manuscript received 4 May 2015; published 26 May 2015)

In this paper we present an atomic-resolution electron microscopy study of superlattices (SLs) where the colossal magnetoresistant manganite $\text{La}_{0.67}\text{Ca}_{0.33}\text{MnO}_3$ (LCMO) and the high critical temperature superconducting cuprate $\text{La}_{1.85}\text{Sr}_{0.15}\text{CuO}_4$ (LSCO) are combined. Although good quality epitaxial growth can be achieved, both the choice of substrate and the relatively large lattice mismatch between these materials (around 2%) have a significant impact on the system properties [*Phys. C* **468**, 991 (2008); *Nature (London)* **394**, 453 (1998)]. Our samples, grown by pulsed laser deposition, are epitaxial and exhibit high structural quality. By means of cutting-edge electron microscopy and spectroscopy techniques we still find that the epitaxial strain is accommodated by a combination of defects, such as interface steps and antiphase boundaries in the manganite. These defects result in inhomogeneous strain fields through the samples. Also, some chemical inhomogeneities are detected, up to the point that novel phases nucleate. For example, at the LCMO/LSCO interface the ABO_3 -type manganite adopts a tetragonal LSCO-like structure forming localized layers that locally resemble the composition of $\text{La}_{2/3}\text{Ca}_{4/3}\text{MnO}_4$. Structural distortions are detected in the cuprate as well, which may extend over lateral distances of several unit cells. Finally, we also analyze the influence of the substrate-induced strain by examining superlattices grown on two different substrates: $(\text{LaAlO}_3)_{0.3}(\text{Sr}_2\text{AlTaO}_6)_{0.7}$ (LSAT) and LaSrAlO_4 (LSAO). We observe that SLs grown on LSAT, which are nonsuperconducting, present reduced values of the c axis compared to superlattices grown on LSAO (which are fully superconducting). This finding points to the fact that the proper distance between copper planes in LSCO is essential in obtaining superconductivity in cuprates.

DOI: [10.1103/PhysRevB.91.205132](https://doi.org/10.1103/PhysRevB.91.205132)

PACS number(s): 73.21.Cd, 68.37.Ma, 74.78.Fk, 75.70.Cn

I. INTRODUCTION

Transition-metal (TM) oxides exhibit a rich variety of behaviors ranging from high critical temperature superconductivity (HTCS) in cuprates to colossal magnetoresistance (CMR) in manganites [1–4]. These physical phenomena and the diverse phase transitions associated with them strongly depend on subtle changes in driving parameters, such as temperature, magnetic/electric field, pressure, and particularly, on the local crystal structure [3,4]. A large number of reports have been devoted to analyze the impact of minor structural distortions on high- T_c superconductivity. The effects of hydrostatic pressure or uniaxial strains have been extensively analyzed [5,6]. Particular attention has been paid to epitaxial strain in thin films, a most important source of lattice distortions and defects, which may have effects comparable to hydrostatic pressures of several gigapascals [7]. For example, it has been shown that a small in-plane compressive strain in $\text{La}_{1.85}\text{Sr}_{0.15}\text{CuO}_4$ (LSCO) HTCS thin films can result in a substantial increase in critical temperature, with reported values even higher than the bulk material [2,8]. Such changes in T_c may depend quite anisotropically on the structure. As a matter of fact, in many HTCS compounds $\partial T_c/\partial p_a > 0$ while $\partial T_c/\partial p_c < 0$, where T_c is the superconducting transition temperature and p_a and p_c denote the uniaxial pressures along the crystallographic a axis (parallel to the CuO_2 planes) and c axis (perpendicular to CuO_2 planes), respectively [2]. It was also shown that chemical doping, or also increasing the oxygen content, can change the superconducting properties of thin films of La_2CuO_4 [9], which underlines the high potential for structural and chemical tunings in these oxides.

Epitaxial mismatch strain in thin superconducting films can be modified through a proper choice of the substrate or also through the growth of superlattices where the cuprate is combined with a different material. This scenario provides further complexity via the interplay between different phenomena. Special attention has been paid to the combination of a superconducting cuprate with a ferromagnetic (FM) manganite. Such systems allow the study of antagonistic superconducting and ferromagnetic order parameters, giving rise to exotic behaviors. A prominent example of a resulting effect can be found in the magnetic proximity effect which gives rise to a strong suppression of the FM moment of the Mn ions on the manganite side of the interface and yet a small induced FM moment of the Cu ions (that is antiparallel to the one of Mn) on the cuprate side [10–17]. The systems that are studied in most cases are superlattices (SLs) combining the cuprate $\text{YBa}_2\text{Cu}_3\text{O}_{7-x}$ and the manganite $\text{La}_{1-x}(\text{Sr,Ca})_x\text{MnO}_3$ since the similarity of their lattice constants results in sharp and coherent epitaxial interfaces [12,18].

LSCO lacks the CuO chain charge reservoir, so the study of the effects of strain in LSCO thin films may shed some extra light on the impact of small structural distortions on superconductivity of the single CuO_2 planes. However, SLs combining manganites and LSCO have not been studied so often. The epitaxy in these systems is hindered by both the relatively large lattice mismatch ($>2\%$) and by the oxygen nonstoichiometry. In our previous work, we have shown that epitaxial and stoichiometric SLs of $\text{La}_{1.85}\text{Sr}_{0.15}\text{CuO}_4/\text{La}_{2/3}\text{Ca}_{1/3}\text{MnO}_3$ can be grown by pulsed laser deposition in a N_2O -rich atmosphere [19]. These SLs

exhibit both ferromagnetism and superconductivity with a superconducting critical temperature $T_c = 36$ K in the cuprate and a ferromagnetic Curie temperature of $T \approx 200$ K in the manganite. Our SLs were grown on LaSrAlO_4 (LSAO) substrates, which impose a small compressive strain on the LSCO film and are the best choice for increasing T_c in LSCO thin films [2,8]. But high quality epitaxy can also be achieved in SLs grown on $(\text{LaAlO}_3)_{0.3}(\text{Sr}_2\text{AlTaO}_6)_{0.7}$ (LSAT), a substrate with a lattice parameter similar to that of $\text{La}_{2/3}\text{Ca}_{1/3}\text{MnO}_3$ (LCMO) (i.e., larger than the in-plane constants of LSCO). In the present study we examine the effects of epitaxial strain in LSCO/LCMO superlattices, paying attention to the role of different underlying substrates (LSAO and LSAT) and identify the complex strain release mechanisms. The SLs presented here consist of eight, nine, and ten LSCO/LCMO bilayers (BLs) where the first layer deposited on the substrate is always LSCO. LCMO crystallizes in the orthorhombic $Pbnm$ cell with a pseudocubic distance of $a_{\text{PC}} = 3.86$ Å [20]. Meanwhile, LSCO crystallizes in a tetragonal K_2NiF_4 -like crystal unit cell with an in-plane parameter $a_{\text{T}} = 3.78$ Å and an out-of-plane lattice constant of $c = 13.26$ Å [21]. The difference between $a_{\text{PC}} = 3.86$ and $a_{\text{T}} = 3.78$ Å exceeds 2%, giving rise to a considerable lattice mismatch between LSCO and LCMO layers. We show that the large lattice mismatch between LSCO and LCMO is accommodated either by interface steps and antiphase boundaries in the orthorhombic LCMO and/or by complex relaxations taking place over several lateral lattice distances in the tetragonal LSCO layer. Although the epitaxy is locally good, we find that the lateral coherence is limited to 20–50 nm approximately. The strain induced by the underlying substrate has also been modified by using two different materials: one with a very good match to the superconductor LSCO and another one with in-plane lattice constants similar to LCMO. On one hand, LSAO, which exhibits a K_2NiF_4 -like crystal structure, just like LSCO, with an in-plane lattice parameter value of $a = 3.756$ Å, close enough to LSCO, and out-of-plane $c = 12.63$ Å [22]. On the other hand, LSAT, which has a cubic crystal cell with $a_{\text{T}} = 3.87$ Å, very similar to that of LCMO [23]. As a result, the strain on the first LSCO layer is very small in LSAO-grown samples (compressive strain -0.6%) but considerably larger in superlattices on LSAT (tensile strain $+2.4\%$).

II. EXPERIMENT

The $\text{La}_{1.85}\text{Sr}_{0.15}\text{CuO}_4/\text{La}_{2/3}\text{Ca}_{1/3}\text{MnO}_3$ superlattices were grown by pulsed laser deposition in N_2O -rich atmosphere as described in Ref. [19]. Cross-sectional high-resolution scanning transmission electron microscopy observations were carried out in an aberration-corrected JEOL JEM-ARM200 CF, operated at 200 kV and equipped with a cold field emission gun and a Gatan quantum electron energy-loss spectrometer (EELS). All images presented here were obtained using a high-angle annular dark field (HAADF) detector, a technique also known as Z-contrast imaging. For this technique, the scattering cross section is given by Rutherford's law, i.e., the intensity of every atomic column is roughly proportional to the square of the atomic number Z [24]. The contrast associated with heavier elements, such as La or Sr, is brighter, whereas lighter heavy elements, such as Cu or

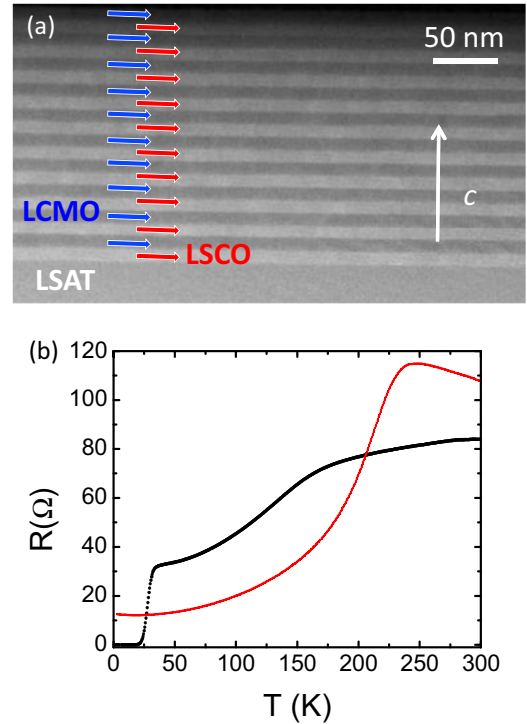


FIG. 1. (Color online) (a) Low magnification HAADF image of a $[\text{LSCO}/\text{LCMO}]_{\text{ten bilayers}}/\text{LSAT}$ superlattice. (b) Resistivity curve of a $[\text{LSCO}/\text{LCMO}]_{\text{eight bilayers}}/\text{LSAT}$ superlattice (red) and a similar sample grown on LSAO (black).

Mn, appear darker. The O atoms, being light and close to the heavier columns, are usually not visible in the HAADF images. Strain field analysis in the images was carried out using the commercial script “peak pairs analysis” developed by “HREM Research, Inc.” Random noise in the EELS data was removed by means of principal component analysis [25]. EELS elemental mapping was performed by integrating the signals under the characteristic elemental edges after background subtraction using a power law. The integration windows were typically around 20–30-eV wide. The manganese L_{23} intensity ratio was calculated using the second derivative method [26]. The specimens were prepared by conventional methods of grinding and Ar-ion milling.

III. RESULTS AND DISCUSSION

Figure 1(a) shows a low magnification HAADF image of a SL grown on a LSAT substrate consisting of ten LSCO (bright) /LCMO (dark) bilayers. The layers and interfaces are flat over long lateral distances, on the order of a micron, just as we found previously in SLs grown on LSAO [19]. The presence of major secondary phases or precipitates was not detected. Although LSCO/LCMO superlattices on LSAO are superconducting [16], LSAT grown superlattices are not. Figure 1(b) shows the resistivity versus temperature curve of an eight-bilayer-thick SL grown on LSAT (red) and on LSAO (black) grown under similar conditions. No fingerprint of a superconducting transition is detected down to 2 K in these superlattices grown on LSAT.

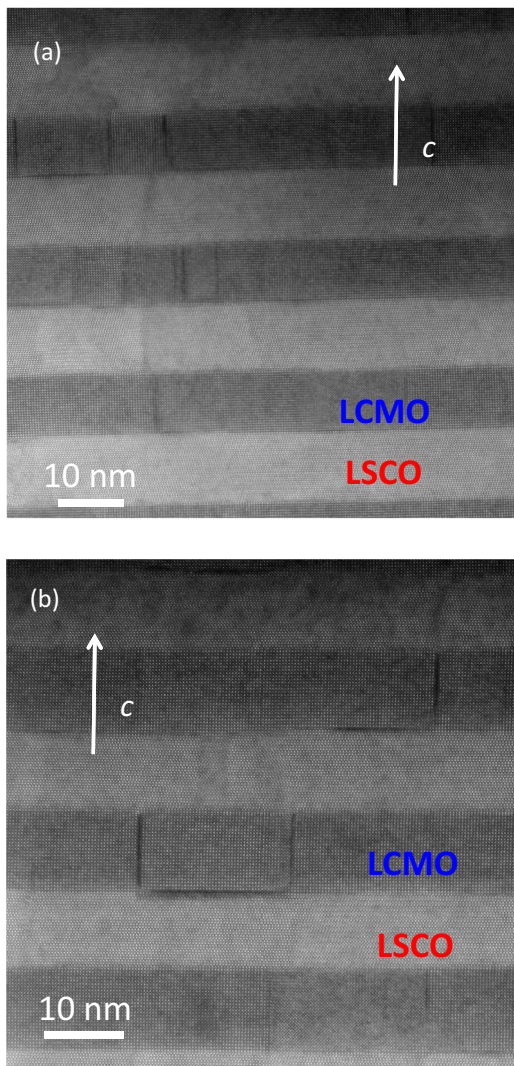


FIG. 2. (Color online) HAADF images of LSCO/LCMO superlattices grown on (a) LSAO and (b) LSAT. $\text{La}_{2/3}\text{Ca}_{1/3}\text{MnO}_3$ layers are dark whereas $\text{La}_{1.85}\text{Sr}_{0.15}\text{CuO}_4$ layers are bright.

Higher magnification images, along with spectroscopic imaging, allow the study of the interfacial structure in detail. Figure 2(a) exhibits an image of a LSCO/LCMO superlattice grown on LSAO, whereas Fig. 2(b) shows an image of a similar sample grown on LSAT. The bright and dark layers correspond to LSCO and LCMO, respectively. Dark vertical stripes can be seen within the LCMO layers. These features are antiphase boundaries (APBs), which, as we will show, stem from interfacial steps. These extended defects, which appear in LCMO layers, have a lateral spacing of 20–50 nm. In fact, 20 nm along the *ab* plane contain approximately 50 perovskite unit cells, which is basically the number of cubic blocks needed to neutralize a 2% mismatch via the introduction of an edge dislocation or some other extended defect. It is likely that these defects help accommodating the strain ensuing from the lattice mismatch. However, we see that the APBs in LCMO are less frequent than one would expect for full mismatch strain accommodation. APBs can also propagate through the cuprate layer (or, at least, the strain fields associated with these

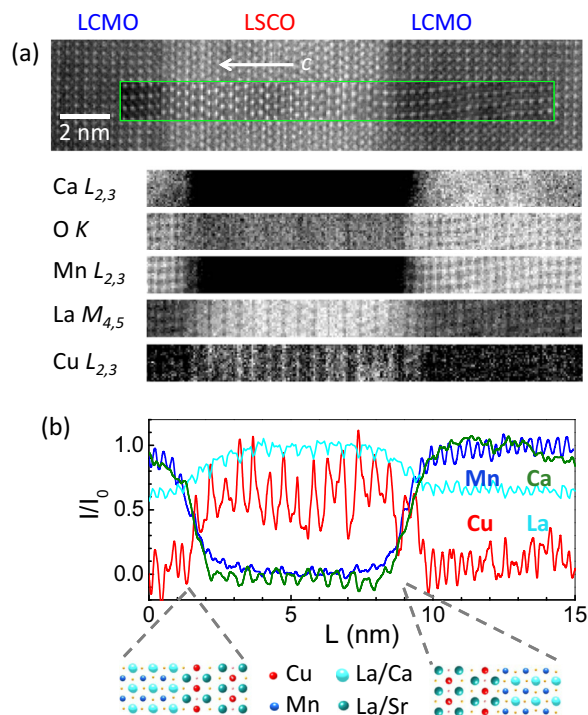


FIG. 3. (Color online) Atomic-resolution EELS of the LCMO/LSCO/LCMO stacking. (a) Atomic-resolution HAADF image with the area where an EEL spectrum is acquired indicated by a green rectangle. The interface on the right is the closest one to the substrate. The inset shows the simultaneously acquired ADF signal. Some spatial drift is visible. From top to bottom, elemental EELS maps for Ca, O, Mn, La, and Cu. (b) Line profiles obtained from averaging laterally the normalized intensities corresponding to the maps above. Ca (green), Mn (blue), La (cyan), and Cu (red) normalized signals are shown. The atomic structures proposed for both interfaces are shown below (not to scale).

extended defects can), and an inhomogeneous distribution of strain fields can be detected within the LSCO layers.

Apart from these localized defects, coherent interfaces and epitaxial growth are observed, such as the interfaces depicted in the atomic-resolution HAADF image in Fig. 3(a) for a LCMO/LSCO/LCMO stacking. EEL spectrum imaging was used to ascertain the interface structure and to probe any chemical disorder (e.g., interdiffusion). A green rectangle marks the area where an atomic resolution EEL spectrum image was taken. The inset shows the ADF signal acquired simultaneously with the spectrum image. Minor spatial drift is observed. Immediately below, a number of elemental maps associated with the different elements of interest are presented (from top to bottom: Ca, O, Mn, La, and Cu signals are displayed). These maps were produced through integration of the signals under the $\text{Ca } L_{2,3}$, $\text{O } K$, $\text{Mn } L_{2,3}$, $\text{La } M_{4,5}$, and $\text{Cu } L_{2,3}$ edges, respectively, after background subtraction using a power law. Normalized line traces across these elemental maps, averaged along the interface plane, are plotted in Fig. 3(b). These profiles can be used to give an upper estimate of the interface chemical width (an actual quantification is hindered by the beam broadening due to dynamical scattering and by the presence of surface amorphous

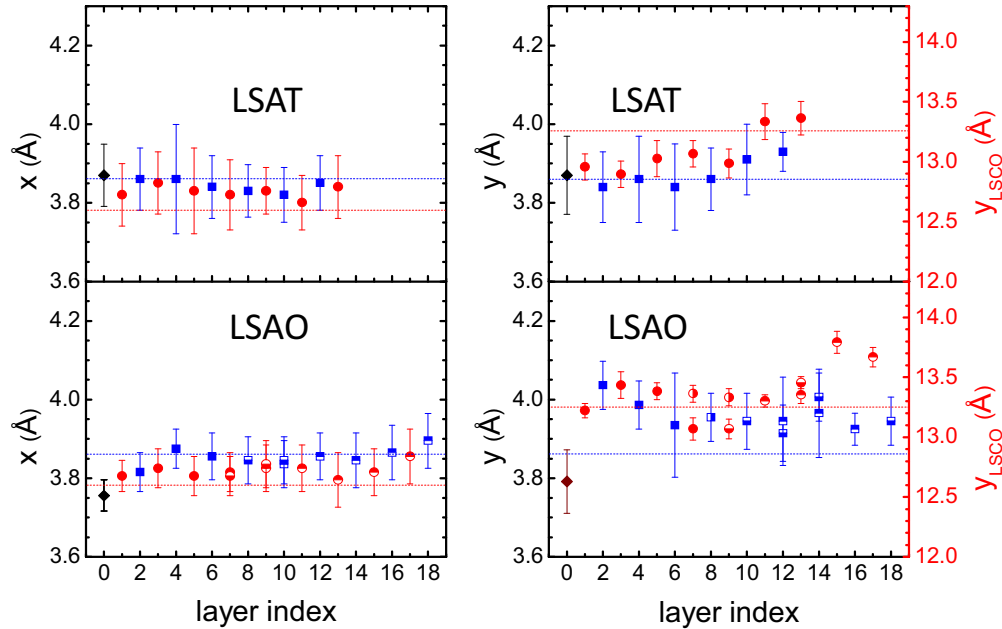


FIG. 4. (Color online) Lattice parameters of LSCO/LCMO superlattices grown on LSAT (top) and LSAO (bottom). x and y stand for distances along the a and c axes, respectively (for LCMO, $x = a_{\text{PC}}$ is the pseudocubic lattice constant). Blue squares and red circles stand for the parameters of the LCMO and LSCO layers, respectively. Different symbols stand for different images analyzed. Diamonds stand for the substrate. The right (red) axis marks the c lattice distances. Horizontal dashed lines mark the values of bulk lattice constants for LCMO (blue) and LSCO (red).

layers which originate from the ion milling process). This width can be evaluated from the 75% to 25% drop in the normalized intensities across the interfaces. This way, we obtain values between 0.5 and 1 nm, which correspond to about two perovskite blocks. Since these are the estimates of the upper limits, we can conclude that the interfaces are very sharp and little chemical interdiffusion is present. It is also worth noting that these profiles exhibit the typical oscillations associated with atomic-resolution contrast and permit locating the corresponding Mn, La, Ca, and Cu atomic planes. Even the noisy Cu signal (the intensity of the Cu $L_{2,3}$ edge is relatively low when compared to the other edges analyzed here) exhibits well-defined maxima at the positions of the CuO_2 -atomic plane, right in between the La/Sr double layers. By looking at the atomic-resolution maps and the averaged profiles we can reconstruct the atomic stacking across both the LSCO top (left) and bottom (right) interfaces. Nonsymmetric interface structures are observed in this sample as is summarized in the sketch below (not to scale). For the LSCO/LCMO interface on the left, a MnO_2 layer faces two heavy-atom planes (La/Ca and La/Sr) in a $\cdots\text{MnO}_2\text{-La/CaO-La/SrO-CuO}_2\cdots$ sequence. We will call this arrangement the “type-1” interface. However, for the interface on the right a different stacking is observed. Here, a MnO_2 plane faces a La/SrO atomic plane, which is followed by a CuO_2 plane. Therefore, the stacking across the interface from left to right is $\cdots\text{-CuO}_2\text{-La/SrO-MnO}_2\text{-La/CaO}\cdots$ hence the neighboring MnO_2 and CuO_2 atomic planes share the apical oxygen atom from their respective oxygen octahedra. We will call this stacking sequence the “type-2” interface. No noticeable charge transfer from LCMO to LSCO was detected in either case (type-1 or type-2 interface). The manganese L_{23} ratio, widely used to probe the oxidation state

of this transition metal [27,28], does not exhibit statistically significant fluctuations across the LCMO layers.

Despite the high structural quality of the superlattices, occasional defects are also detected. As reported in other complex oxide systems, these defects are very likely related to the release of mismatch strain. In order to get some insight on the local distribution of strains we have analyzed the evolution of lattice constants (in plane and out of plane) through the stacking. This task can be achieved through the quantification of atomic column positions in atomic-resolution images. Although Fig. 4 shows the evolution with increasing thickness (layer index) of both the in-plane (x) and the out-of-plane (y) lattice distances, measured between the heavy columns (La/Sr, La/Ca) in our HAADF images for samples grown on both LSAT (top) and LSAO (bottom). Horizontal dashed lines mark the bulk lattice parameter values for LCMO (blue) and LSCO (red). In order to remove the errors arising from any sample’s spatial drift during the image acquisition, we have acquired images with two different scanning orientations (mutually perpendicular). We have analyzed both sets and present here the averaged results. In LCMO, both x and y lattice constants correspond to the pseudocubic cell parameter (nominally $a_{\text{PC}} = 3.86 \text{ \AA}$), pointing to a relaxed structure relatively free of strain. For LSCO and LSAO, x and y are the principal axes of their tetragonal crystal cell, the a and c lattice constants, respectively. In Fig. 4, x and y are presented as a function of increasing layer index where the substrate (black point) is zero, odd numbers stand for LSCO (red symbols), and even numbers stand for LCMO layers (blue symbols). The in-plane constant x is always close to 3.86 \AA in SLs grown on both LSAT and LSAO, although it seems to be slightly smaller in the latter. A rather minor increase in the in-plane

lattice parameter of LSAT samples is detected near the sample surface. However, it is too close to the error bars to be deemed significant. Still, it is worth noting that it could be due to several factors: Perhaps a gradient in the oxygenation of the layers or, more likely, it may point out a partial relaxation of strain through the sample thickness. The out-of-plane constants γ are more inhomogeneous, but in LCMO they are still close to the pseudocubic value of $\gamma = 3.86 \text{ \AA}$. On the other hand, the LSCO out-of-plane lattice parameter on LSAT seems to be noticeably smaller ($\gamma = 13.0 \text{ \AA}$) than the bulk value $c = 13.26 \text{ \AA}$, probably due to the in-plane tensile strain imposed by the substrate, and they increase slightly towards the sample surface (perhaps also a result of partial strain relaxation). For SLs grown on LSAO the c axis is rather close to the bulk value, probably due to the very small compressive strain imposed by the substrate on the first LSCO layer [2]. Still, a slight enlargement of the c axis near the surface is observed as well.

All these findings suggest the presence of an inhomogeneous distribution of strains and hint to a partial relaxation via the introduction of defects across the sample thickness. Further information on the type and density of defects can be obtained through a closer look at the Z -contrast images in Fig. 2. Dark vertical stripes can be seen within the LCMO layers. These features are APBs, which, as we will show, stem from interfacial steps. These extended defects, which appear in LCMO layers, have a lateral spacing of 20–50 nm. In fact, 20 nm along the ab plane contain approximately 50 perovskite unit cells, which is basically the number of cubic blocks needed to neutralize a 2% mismatch via the introduction of an edge dislocation or some other extended defect. It is likely that these defects help accommodating the strain ensuing from the lattice mismatch. However, we see that the APBs in LCMO are less frequent than one would expect for full mismatch strain accommodation. APBs can also propagate through the cuprate layer (or, at least, the strain fields associated with these extended defects can), and an inhomogeneous distribution of strain fields can be detected within the LSCO layers as well. The strain maps in Fig. 5 have been obtained from a 360-nm^2 -wide region of a SL grown on LSAT that contains several defects. Figure 5(a) displays the HAADF image containing several antiphase boundaries within the LCMO layers. Panels (b) and (c) depict the in-plane $\epsilon_{xx} = \partial u_x / \partial x$ and out-of-plane $\epsilon_{yy} = \partial u_y / \partial y$ strains, respectively. Here, x and y correspond again to the in-plane (horizontal) and out-of-plane (vertical) directions, respectively, whereas u_x and u_y are the coordinates of the bright (La/Ca and La/Sr) atomic columns in the layers. The choice of color (related to the distribution of positive or negative strains) in this representation depends on the region taken as the reference to calculate the relative strains. In our case, the reference has been chosen within the second LSCO layer. Therefore, the strain maps may exhibit quite different contrasts when comparing LCMO and LSCO layers. This contrast, particularly visible in the ϵ_{yy} map, is a consequence of different crystalline structures of LCMO (orthorhombic $Pbnm$) and LSCO (tetragonal $I4/mmm$). In this case, the relative changes taking place within individual layers are the ones which bare actual relevance. In both maps large strain fields are observed around the APBs in LCMO. Additionally, distorted regions are observed in the LSCO layers as well.

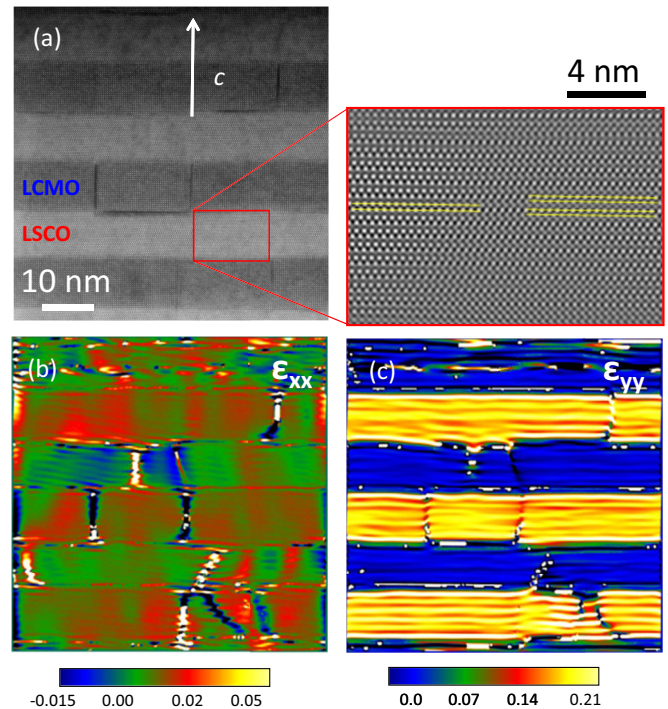


FIG. 5. (Color online) (a) Intermediate magnification HAADF image of a LSCO/LCMO superlattice, together with strain maps: (b) ϵ_{xx} and (c) ϵ_{yy} . The direction of the crystallographic c axis is marked with a white arrow. The inset in (a) is a zoom into the LSCO region highlighted with a red rectangle.

These defects in LSCO are shown in the right panel of Fig. 5(a) in the enlarged region of the third LSCO layer. In order to remove the noise, we have filtered the original HAADF image by masking the principal reflection spots in the Fourier transform. An APB can be seen with a tilt component with respect to the electron beam: The rock-salt planes on the left side (marked with double yellow lines) are shifted vertically with respect to the atomic planes on the right (two double yellow lines).

In order to explore the strain-induced defects at the atomic level, we have analyzed high magnification images of a LSCO/LCMO superlattice grown on LSAT, such as the one shown in Fig. 6. The interfaces are highly coherent as a result of the atom-on-atom growth. However, two interface steps are clearly observable. The first one is on the bottom interface (marked with a yellow arrow). An antiphase boundary (darker contrasts) crosses the LCMO layer all the way up to this step. The mismatch between the LCMO crystal structure on the right and on the left of the APB is evident: The atomic planes are displaced by half a unit block from each other along the growth direction (hence, MnO_2 planes from the left meet LaO planes coming from the right side). The boundary planes are quite sharp and in general have a well-defined orientation with the pseudocubic structure (we see them often running perfectly parallel to the electron-beam direction without a tilt component). Another interfacial step is located at the top interface just above the previous (highlighted with a yellow rectangle). The APBs are not propagating into the LSCO layers, the associated strain fields are noticeable and, as a matter of fact, the second interface step is just above the first one on the next (top) interface. We have marked this one with a yellow rectangle

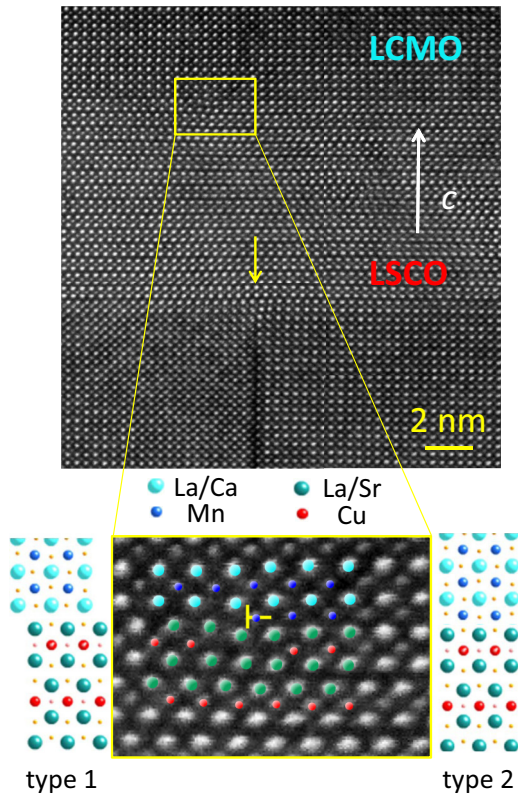


FIG. 6. (Color online) High-resolution HAADF image of a LCMO/LSCO/LCMO sequence in a nine-BL sample grown on LSAT. A step in the lower interface, associated with an APB in the LCMO layer, is marked with a yellow arrow. A yellow rectangle highlights another step at the top interface, which has been magnified below. Models of the surrounding structure are shown on corresponding sides. The color code for the different atomic columns is as follows: Mn (blue), Cu (red), La/Ca (cyan), and La/Sr (green).

and shown a magnified view below. The sketches on both sides of the step show the corresponding crystal structures. On the lower side of the interface, we have the LSCO regular structure. LSCO crystallizes in a K_2NiF_4 -like structure which appears as pseudocubic perovskite blocks displaced laterally by half a cell. The La/Sr columns appear brighter with dimmer Cu columns in between. On the top we have the perovskite LCMO (again, bright columns are the heavy La/Ca whereas Mn columns appear the dimmest). The interface terminations are different on both sides of the step. On the right we have the so-called type-2 structure with neighboring MnO_2 and CuO_2 rows sharing apical oxygen atoms. Meanwhile, on the left end we find the type-1 interface with the typical rock-salt-like stacking. The extra MnO_2 semiplane coming from the right side and finishing at the interface step is marked on the magnified image. Interestingly, some Cu columns around the defect seem to be missing in the image, suggesting that the large strain around these defects may give rise to intense fluctuations in the local composition. We will come back to this point later. For now, it is clear that large local deformations of the crystal lattice are observed around this defect which take distances of a few nanometers to relax. Such an arrangement of upper and lower interfaces results in

asymmetric (left) and symmetric (right) LCMO/LSCO/LCMO interfaces. Therefore, distributions of different (symmetric and asymmetric) types of interfaces in cuprate/manganite heterostructures are the natural consequence of the presence of defects induced by the large mismatch of their respective unit cells.

Such intense nanoscale fluctuations of strain have been reported to determine the pinning properties of high- T_c superconducting thin films [29]. Local strains have been shown to produce segregation of different chemical species in order to minimize energy and relax the structure (e.g., Ca segregation in yttrium barium copper oxide dislocation cores) [30]. Hence, it is of the utmost importance to understand what happens at the atomic scale around these defects especially if strain can affect the local chemical balance. Unexpected effects of strain can be found associated with them, which can affect even the local chemical balance, as we have already mentioned. Figure 7 presents the compositional analysis of a LCMO layer containing both an APB and the interface steps, such as the example above. Figure 7(a) shows an atomic-resolution HAADF image with the APB vertical dark stripe across the LCMO layer. Also, a horizontal black stripe a few nanometers long is observed on the LSCO side of the interface, stemming from the step and running towards the left of the step. Such regions are seen less frequently than vertical dark stripes, but they are not uncommon. The reduced ADF signal on these stripes may suggest a lower average Z number resulting from a local change in chemical composition. In order to investigate this possibility, we acquired atomic-resolution EEL spectrum images around areas, such as the one marked with a yellow square in Fig. 7(a). Figure 7(b) depicts the ADF signal acquired simultaneously with the spectrum image. Although some spatial drift is present, atomic-resolution contrast is observable. The whole region of the APB boundary threading across the LCMO layer from top to bottom exhibits the typical dark contrast. Part of the horizontal dark stripe is also included. Atomic-resolution elemental maps obtained from integrating the signals under the (c) Ca $L_{2,3}$, (d) La $M_{4,5}$, (e) Cu $L_{2,3}$, (f) O K , and (g) Mn $L_{2,3}$ edges are shown below. All maps, except for the noisy Cu, exhibit atomic resolution, and the local structure can be analyzed. The most striking feature is the enhanced Ca concentration, along with a weakened La signal, right on the top of dark areas associated with both the APB and the horizontal dark stripe in the LSCO layer in Fig. 7(a). The APB has a width of two atomic planes, rich in Ca and La deficient. The measured enhancement of the Ca signal on the vertical APB is a sign that this defect is made of rock-salt-like CaO planes as also observed in Ref. [31]. As for the horizontal stripe, approximately four Ca-rich planes can be counted. Contrary to La, neither the O nor the Mn signals seem reduced in these areas. Actually, the relative local O content seems higher within the defective area on the LSCO side of the interface. Also, two Mn-rich planes can be observed in this same region, spaced 6.64 Å. This is exactly half a unit cell of bulk LSCO, i.e., the distance that separates CuO_2 planes along the c axis. Simultaneously, the Cu signal is reduced, so we can conclude that the Cu ions in LSCO are being replaced by Mn ions to form a different phase of nanometric dimensions. The nucleation of this phase is very likely responsible for triggering a local release of strains. If one considers the enhanced Ca

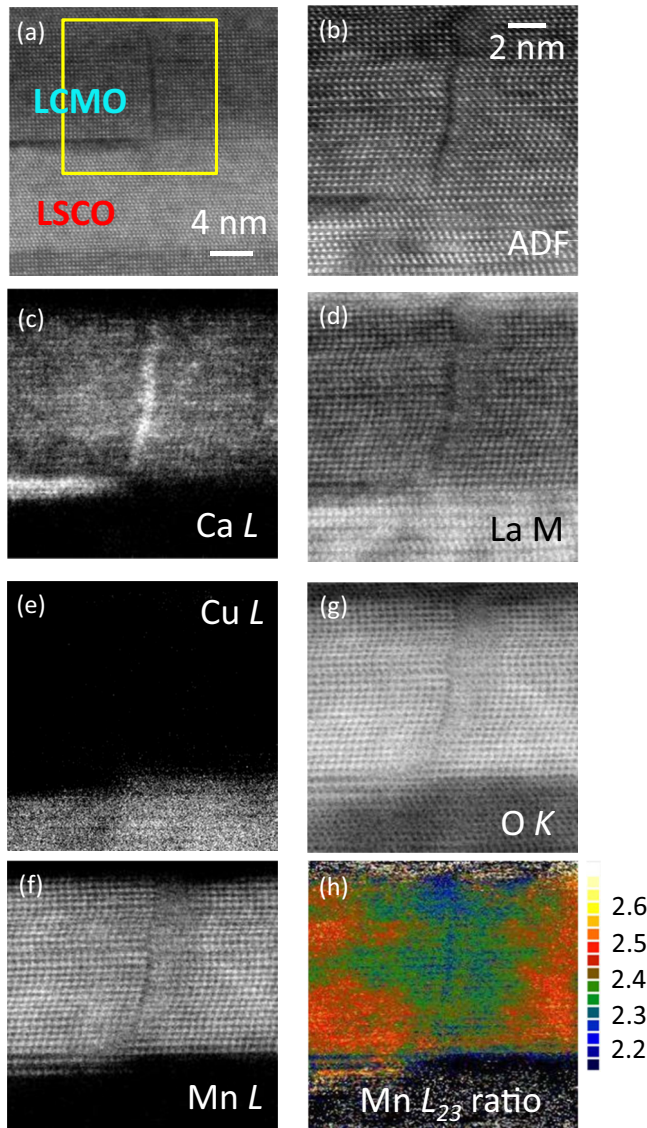


FIG. 7. (Color online) Atomic-resolution EELS maps across a LCMO layer in a LCMO/LSCO superlattice, including an APB. (a) HAADF image of the region where an EEL spectrum image was acquired (area highlighted with a yellow rectangle). (b) Simultaneous ADF signal. The next panels show the different elemental maps obtained from integrating the (c) Ca $L_{2,3}$, (d) La $M_{4,5}$, (e) Cu $L_{2,3}$, (f) O K , and (g) Mn $L_{2,3}$ edge signals. (h) Manganese $L_{2,3}$ ratio across the LCMO layer (only meaningful in the regions where some Mn signal is actually present).

signal, the chemical composition within the horizontal defect appears to resemble a $\text{La}_{1-x}\text{Ca}_{1+x}\text{MnO}_4$ -like phase, i.e., a manganite with a structure similar to the surrounding LSCO. A phase like that to the best of our knowledge has not been reported to exist in bulk due to large mismatch between the sizes of the La and Ca ions. Although the substitution of La by Ca can be achieved in the single perovskite ABO_3 and in the double-layer perovskite $\text{A}_3\text{B}_2\text{O}_7$, the small size of the Ca ion hinders the creation of a single-layer perovskite A_2BO_4 , such as our $\text{La}_{1-x}\text{Ca}_{1+x}\text{MnO}_4$. However, nanometric pockets of such a compound are created here by the local strain field and are acting as a strain-relief mechanism.

Back to the issue of whether the APB region may present some extra charge, the electronic properties of these planes can be analyzed by looking at the Mn $L_{2,3}$ edge fine structure. In particular, the $L_{2,3}$ intensity ratio in transition metals is a parameter commonly used to determine their oxidation states [27,28]. Specifically, it has been found that the manganese $L_{2,3}$ ratio decreases with an increasing Mn oxidation state [32]. Figure 6(h) shows the two-dimensional map of the manganese $L_{2,3}$ intensity ratio for this spectrum image. Within the LCMO layer, a few nanometers far from the APB the Mn $L_{2,3}$ ratio exhibits values close to 2.5 [orangish areas in Fig. 6(h)]. This value is in excellent agreement with the reported value of $\text{Mn}^{+3.3}$. This would be the oxidation state expected for our nominal composition of $\text{La}_{2/3}\text{Ca}_{1/3}\text{MnO}_3$. However, the Mn $L_{2,3}$ ratio decreases dramatically on the APB plane, down to values of 2.2. According to [32], a value of $L_{2,3} = 2.2$ points to a manganese oxidation state close to $\text{Mn}^{+3.66}$, in good agreement with an enhanced Ca (decreased La) content on the antiphase boundary. On the other hand, in the nanopocket at the LSCO interface, values of the Mn $L_{2,3}$ ratio close to 2.5 are found again—see the two orange rows associated with the two Mn-rich planes in the horizontal defect. This finding suggests that the Mn oxidation state is approximately $\text{Mn}^{+3.33}$ on these planes, which would be expected for the $\text{La}_{2/3}\text{Ca}_{1/3}\text{MnO}_3$ stoichiometry. However, the distance between adjacent Mn planes in the nanopocket is not compatible with a perovskite crystal structure. Assuming the LSCO (K_2NiF_4) structure, this phase could be identified as $\text{La}_{2/3}\text{Ca}_{4/3}\text{MnO}_4$. This unexpected composition, not known in bulk form, may nucleate thanks to the fact that manganese and calcium atoms are being deposited on top of LSCO, acting as a host template of the K_2NiF_4 type and assemble into a similar arrangement. Such a structural assembly must therefore be a direct consequence of the considerable strain produced near the interface step below the APB [Figs. 6(a) and 6(b)]. A similar effect was recently observed in $\text{La}_{2/3}\text{Sr}_{1/3}\text{MnO}_3$ thin films grown on LSAO [33] where a nominal $\text{La}_{2/3}\text{Sr}_{1/3}\text{MnO}_3$ thin film reassembles into both LaSrMnO_4 and LaAlO_3 structures in order to accommodate the strain imposed by the LSAO substrate. The particularity of our case is that the mismatch strain can stabilize a compound that does not exist in bulk.

Finally, we also want to discuss the influence of the substrate and comment on the features of the substrate-LSCO interface. As already mentioned, we have used two different substrates in this study: LSAO matches relatively closely the in-plane lattice parameters of LSCO, whereas LSAT is a better match to LCMO. We have seen that the structure, type, and distribution defects found in the samples grown on both LSAO and LSAT are very similar. Yet, SLs grown on LSAO present a superconducting transition (and it is well known in literature that LSAO is a good choice of substrate for the growth of LSCO thin films with optimal properties). Meanwhile, superlattices grown on LSAT do not exhibit superconductivity. Our study shows that the main structural difference between those two is the approximately 1.5% decrease in the c lattice parameter of LSCO on LSAT (Fig. 4). This means that the CuO_2 planes in SLs grown on LSAT are much closer to each other than the bulk, highlighting the important role of this distance in the mechanism responsible for high- T_c superconductivity. Other interesting features can be

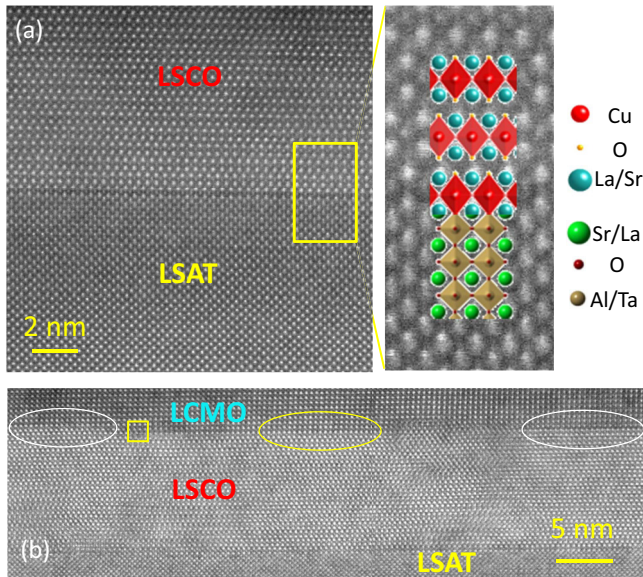


FIG. 8. (Color online) (a) High-resolution HAADF image of the LSCO (top)/LSAT (bottom) interface. The model of the interface is shown on right. Oxygen octahedra are plotted in both LSCO (elongated red octahedra) and LSAT (symmetrical yellow octahedra). (b) First LCMO/LSCO bilayer grown on LSAT. LSCO is strained to match perfectly the underlying LSAT substrate. The upper, LCMO/LSCO interface, shows different terminations in different regions (white and yellow ellipses). A yellow rectangle indicates the interface step separating areas with two different interface stacking sequences.

observed by closely inspecting the LSCO/substrate interface. Figure 8(b) is the atomic-resolution HAADF image of the first LSCO layer (50-nm lateral scale). The lattice mismatch between LSCO and LSAT is large, in principle, but still this image denotes a coherent interface with very high quality epitaxy. The LSCO/LCMO interface on top exhibits features already described in Fig. 6: different terminations (type 1—white ellipses on both lateral sides and type 2—yellow ellipse in the middle) or atomic steps, such as the one highlighted in the yellow square. This shows that the perfectly strained LSCO (at the interface with LSAT) relaxes already in the first LSCO layer, despite being sandwiched between materials with similar lateral lattice constants [$a(\text{LSAT}) = 3.87 \text{ \AA}$ and $a_{\text{PC}}(\text{LCMO}) = 3.86 \text{ \AA}$]. Figure 8(a) exhibits a zoom into the LSCO/LSAT interface with a structural model shown on the right. This dark atomic plane can be identified as a CuO_2

plane because the B -site atom in it displays a contrast similar to the CuO_2 planes in LSCO. Meanwhile, the B -site atomic column in LSAT is much brighter (i.e., heavier). However, this interfacial CuO_2 plane exhibits a darker contrast than the CuO_2 planes in LSCO. This lower intensity could be an effect of a local O deficiency. Since the Cu-O octahedra share their apical atom with the substrate first unit cell, a local interfacial oxygen deficiency may alter the local doping and have an impact on experiments aimed at injecting carriers (e.g., electric-field injection or others).

IV. SUMMARY

We have shown that high quality epitaxial LSCO/LCMO superlattices can be grown on different substrates but that lattice mismatch gives rise to partial relaxation strains through the introduction of structural defects. When LCMO and LSCO are combined, the in-plane lattice parameters tend to be closer to the LCMO values although both materials present some degree of strain. We find that this is the case for superlattices grown on both compressive (LSAO) and tensile (LSAT) substrates. However, the LSCO out-of-plane c axis seems to be further reduced in samples grown on tensile LSAT (13.0 \AA versus a bulk value of 13.26 \AA). This reduced CuO_2 plane to CuO_2 plane distance may be connected to the lack of superconductivity found in these samples. We have also shown that the orthorhombic LCMO layers exhibit APBs associated with interfacial steps located within characteristic lateral length scales of 20–50 nm. These steps and APB defects give rise to inhomogeneous strain fields that can penetrate into tetragonal LSCO. Near the interface steps, a K_2NiF_4 -like crystal structure not stable in bulk nucleates in order to further reduce the local strain. All these findings should be taken into account when trying to explain the superconducting properties of ultrathin LSCO layers sandwiched in between other complex oxides with perovskite structures.

ACKNOWLEDGMENTS

We thank A. Lupini for the DM script used for quantification of the lattice constants (Fig. 4) and M. Watanabe for the plug-in for PCA. M.V. acknowledges discussions with J. Mitchell. N.B. and the electron microscopy performed at the Centro Nacional de Microscopía Electrónica (UCM) were sponsored by the ERC Starting Investigator Award No. STEMOX#239739. The research at the University of Fribourg was supported by the Schweizer Nationalfonds (SNF) Grants No. 200020-140225 and No. 200020-153660.

- [1] H. Sato, *Phys. C* **468**, 991 (2008).
- [2] J.-P. Locquet, J. Perret, J. Fompeyrine, E. Machler, J. W. Seo, and G. Van Tendeloo, *Nature (London)* **394**, 453 (1998).
- [3] A. K. Saxena, *High-Temperature Superconductors* (Springer, Berlin/Heidelberg, 2012).
- [4] E. Dagotto, T. Hotta, and A. Moreo, *Phys. Rep.* **344**, 1 (2001).
- [5] A. A. R. Fernandes, J. Santamaria, S. L. Bud'ko, O. Nakamura, J. Guimpel, and I. K. Schuller, *Phys. Rev. B* **44**, 7601 (1991).

- [6] D. T. Jover, R. J. Wijngaarden, R. Griessen, E. M. Haines, J. L. Tallon, and R. S. Liu, *Phys. Rev. B* **54**, 10175 (1996).
- [7] M. Merz, P. Nagel, C. Pinta, A. Samartsev, H. v. Löhneysen, M. Wissinger, S. Uebe, A. Assmann, D. Fuchs, and S. Schuppler, *Phys. Rev. B* **82**, 174416 (2010).
- [8] H. Sato and M. Naito, *Phys. C* **274**, 221 (1997).
- [9] I. Bozovic, G. Logvenov, I. Belca, B. Narimbetov, and I. Sveklo, *Phys. Rev. Lett.* **89**, 107001 (2002).

- [10] J. Salafranca and S. Okamoto, *Phys. Rev. Lett.* **105**, 256804 (2010).
- [11] J. Salafranca, J. Rincón, J. Tornos, C. León, J. Santamaria, E. Dagotto, S. J. Pennycook, and M. Varela, *Phys. Rev. Lett.* **112**, 196802 (2014).
- [12] C. Visani, J. Tornos, N. M. Nemes, M. Rocci, C. Leon, J. Santamaria, S. G. E. te Velthuis, Y. Liu, A. Hoffmann, J. W. Freeland, M. Garcia-Hernandez, M. R. Fitzsimmons, B. J. Kirby, M. Varela, and S. J. Pennycook, *Phys. Rev. B* **84**, 060405(R) (2011).
- [13] Z. Sefrioui, M. Varela, V. Peña, D. Arias, C. León, J. Santamaría, J. E. Villegas, J. L. Martínez, W. Saldarriaga, and P. Prieto, *Appl. Phys. Lett.* **81**, 4568 (2002).
- [14] Z. Sefrioui, D. Arias, V. Peña, J. E. Villegas, M. Varela, P. Prieto, C. León, J. L. Martinez, and J. Santamaria, *Phys. Rev. B* **67**, 214511 (2003).
- [15] V. Peña, Z. Sefrioui, D. Arias, C. Leon, J. Santamaria, M. Varela, S. J. Pennycook, and J. L. Martinez, *Phys. Rev. B* **69**, 224502 (2004).
- [16] J. Stahn, J. Chakhalian, C. Niedermayer, J. Hoppler, T. Gutberlet, J. Voigt, F. Treubel, H.-U. Habermeier, G. Cristiani, B. Keimer, and C. Bernhard, *Phys. Rev. B* **71**, 140509 (2005).
- [17] G. M. De Luca, G. Ghiringhelli, C. A. Perroni, V. Cataudella, F. Chiarella, C. Cantoni, A. R. Lupini, N. B. Brookes, M. Huijben, G. Koster, G. Rijnders, and M. Salluzzo, *Nat. Commun.* **5**, 5626 (2014).
- [18] V. K. Malik, I. Marozau, S. Das, B. Doggett, D. K. Satapathy, M. A. Uribe-Laverde, N. Biskup, M. Varela, C. W. Schneider, C. Marcelot, J. Stahn, and C. Bernhard, *Phys. Rev. B* **85**, 054514 (2012).
- [19] S. Das, K. Sen, I. Marozau, M. A. Uribe-Laverde, N. Biskup, M. Varela, Y. Khaydukov, O. Soltwedel, T. Keller, M. Dobeli, C. W. Schneider, and C. Bernhard, *Phys. Rev. B* **89**, 094511 (2014).
- [20] G. H. Rao, J. R. Sun, J. K. Liang, and W. Y. Zhou, *Phys. Rev. B* **55**, 3742 (1997).
- [21] R. J. Cava, A. Santoro, D. W. Johnson, and W. W. Rhodes, *Phys. Rev. B* **35**, 6716 (1987).
- [22] R. D. Shannon, R. A. Oswald, J. B. Parise, B. H. T. Chai, P. Byszewski, A. Pajaczkowska, and R. Sobolewski, *J. Solid State Chem.* **98**, 90 (1992).
- [23] B. C. Chakoumakos, D. G. Schlom, M. Urbanik, and J. Luine, *J. Appl. Phys.* **83**, 1979 (1998).
- [24] S. J. Pennycook, *Ultramicroscopy* **30**, 58 (1989).
- [25] M. Bosman, M. Watanabe, D. T. L. Alexander, and V. J. Keast, *Ultramicroscopy* **106**, 1024 (2006).
- [26] G. A. Botton, C. C. Appel, A. Horsewell, and W. M. Stobbs, *J. Microsc.* **180**, 211 (1995).
- [27] T. G. Sparrow, B. G. Williams, C. N. R. Rao, and J. M. Thomas, *Chem. Phys. Lett.* **108**, 547 (1984).
- [28] W. G. Waddington, P. Rez, I. P. Grant, and C. J. Humphreys, *Phys. Rev. B* **34**, 1467 (1986).
- [29] A. Llordés, A. Palau, J. Gázquez, M. Coll, R. Vlad, A. Pomar, J. Arbiol, R. Guzmán, S. Ye, V. Rouco, F. Sandiumenge, S. Ricart, T. Puig, M. Varela, D. Chateigner, J. Vanacken, J. Gutiérrez, V. Moshchalkov, G. Deutscher, C. Magen, and X. Obradors, *Nat. Mater.* **11**, 329 (2012).
- [30] R. F. Klie, J. P. Buban, M. Varela, A. Franceschetti, C. Jooss, Y. Zhu, N. D. Browning, S. T. Pantelides, and S. J. Pennycook, *Nature (London)* **435**, 475 (2005).
- [31] M. L. Ruiz-González, R. Cortés-Gil, A. Torres-Pardo, D. González-Merchante, J. M. Alonso, and J. M. González-Calbet, *Chemistry* **20**, 1237 (2014).
- [32] M. Varela, M. P. Oxley, W. Luo, J. Tao, M. Watanabe, A. R. Lupini, S. T. Pantelides, and S. J. Pennycook, *Phys. Rev. B* **79**, 085117 (2009).
- [33] B. Cui, C. Song, G. Y. Wang, H. J. Mao, F. Zeng, and F. Pan, *Sci. Rep.* **3**, 2542 (2013).